Deep-learning to Predict Perceived Differences to a Hidden Reference Image

Mojtaba Bemana
MPI Informatik

Karol Myszkowski
MPI Informatik

Hans-Peter Seidel
MPI Informatik

Tobias Ritschel
University College London

Abstract

Image metrics predict the perceived per-pixel difference between a reference image $\mathcal{B}$ and its degraded (e. g., re-rendering) version $\mathcal{A}$. We devise a neural network architecture and training procedure that allows predicting the MSE, SSIM or VGG16 image difference $\mathcal{A} \ominus \mathcal{B}$ from the distorted image $\mathcal{A}$ alone, when the reference $\mathcal{B}$ is not observed.

This is enabled by two insights: The first is to inject sufficiently many un-distorted natural image patches, which can be had in arbitrary amounts and are known to have no perceivable difference to themselves. This avoids false positives. The second is to balance the learning, where it is carefully made sure that all image errors are equally likely, avoiding false negatives. Surprisingly, we observe, that the resulting non-paired metric, subjectively, can even perform better than the paired one, as it had to become robust to misalignments. We demonstrate the effectiveness of our approach quantitatively and in a user study, as well as qualitatively, in an image-based rendering application where we predict difference visibility maps.

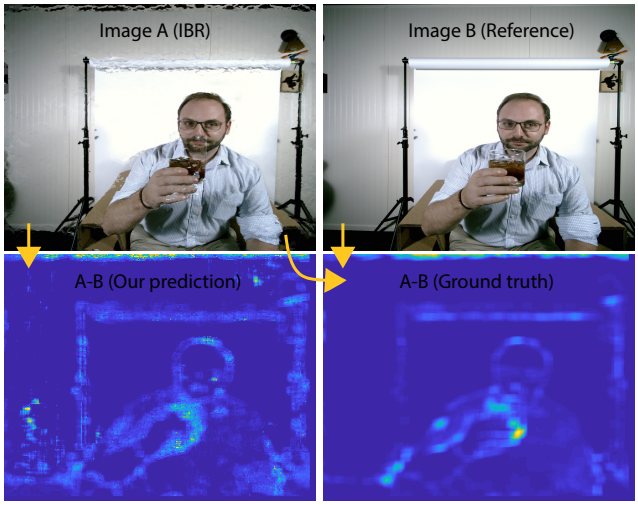

Figure 1. Given an image $\mathcal{A}$ **(top left)** that is a version of a reference $\mathcal{B}$ **(top right)** distorted by IBR artifacts, we predict their difference $\mathcal{A} \ominus \mathcal{B}$ **(lower left)** without observing $\mathcal{B}$. The lower right shows the ground truth difference $\mathcal{A} \ominus \mathcal{B}$. We here show MSE, but other metrics such SSIM and VGG16 are possible.

1. Introduction

Computer vision or graphics experts know their artifacts when they see them. An image-base rendering (IBR) specialist will quickly notice where depth estimation failed, where transparency was not handled or where a highlight did not move correctly. Similarly, in computer graphics, artifacts resulting from Monte Carlo noise in image synthesis producing a feature film or shadow bias [49] in a computer game are easily spotted by domain experts. The assessment typically is not limited to detection, but importantly includes, first, judging magnitude and second, spatial locality. The importance of interacting with errors can be seen from photographs with spatially annotated over- and under-exposition artifacts, as done e. g., by Henri Cartier-Bresson [10]. Remarkably, all this is not achieved by comparing an image to a reference, but by experience and intuition built from knowing what natural images are and how images with artifacts differ. Can we enable a machine to also perform this task?

More formally, we face the challenge illustrated in Fig. 1. Given an image $\mathcal{A}$ that is a distorted version of a reference $\mathcal{B}$ we wish to predict their difference $\mathcal{A} \ominus \mathcal{B}$ without access to $\mathcal{B}$. The lower right shows the ground truth metric response $\mathcal{A} \ominus \mathcal{B}$. This metric could simply be mean square error (MSE, used in Fig. 1), a more perceptual metric like SSIM [48] or even VGG-16 activation differences that are effective as an image metric [40, 52]. Noteworthy, when executing our method on image $\mathcal{B}$ the output is close to zero almost everywhere, i. e., free of false positives. While this is not shown in Fig. 1, Fig. 4 and Tbl. 1 will show positive and negative tests following this protocol in detail.

More particularly, we go beyond the typical mean opinion scores [42] given to uniform distortions such as noise or JPEG compression, and seek to produce localized distortion visibility maps. And most importantly all this without seeing the reference.

Not requiring a reference is useful whenever the original is inaccessible (lost, impossible to compute, unavailable, undefined). Furthermore, it makes the method tolerant to eventual alignment errors which plague other metrics [22]:

if no reference is given, no alignment issues can arise.

We choose to study one specific form of artifacts that arise in image-based rendering (IBR) [30, 14], in particular, when employed for novel-view synthesis from sparse light field (LFs) [25]. It is important in virtual reality and movie production where LFs need to be used for head motion parallax and special effects. It is also important for quality control to have a localized error prediction. In IBR, artifacts are very localized (e. g., around certain depth edges) and creating opinion scoring or even spatio-angular annotated data sets of LF artifacts in a size sufficient for machine learning appears as a daunting task. Our method proceeds without all of this.

Addressing this task, we make use of convolutional neural networks. We will show, how learning this mapping right away, will result in many false positives or false negatives. Instead, two important ingredients come together in our approach. First, as the number of images with artifact is typically limited, we need to augment the data with natural images that are certain to not have artifacts. Second, we suggest a way to find the right balance between natural and distorted training data.

2. Previous Work

In this section we discuss objective image metrics, with special emphasis on those that do not require the undistorted reference image. Then, we briefly characterize IBR-specific artifacts, as well as metrics specialized in their detection, which is the key focus of this work.

Image metrics Image metrics can be categorized into *quality* and *visibility* metrics due to their different functions and applications [9].

Image quality metrics (IQMs) evaluate the distortion magnitude and are typically trained on the mean-opinion score (MOS) data [39, 35] that labels the entire image with as a single quality score. The most commonly used IQMs such as PSNR, CIELAB [53], SSIM and MS-SSIM [47], FSIM [51] are *full reference* (FR) metrics that take as input the reference and distorted images, and compute local differences that are pooled into a global, single quality score. Recently, it has been demonstrated that CNN-based FR-IQMs achieved best performance in predicting MOS data [2, 7]. Zhang et al. [52] employ crowdsourcing and develop a large scale patch-based dataset in two perceptual experiments: (1) two-alternative forced choice (2AFC) on distortion strength, and (2) "same/not same" near-threshold distortion visibility. They train different network architectures and report in each case a much better performance than traditional FR-IQMs in predicting their data from both experiments.

Visibility metrics (VMs) predict the distortion perceptibility for every pixel in the form of visibility maps. VMs are specifically tuned for detecting near-threshold distortions, which is required in many graphics and vision applications that cannot tolerate any perceivable quality reduction and require local information on the distortion positions. To decide on the visibility of such near-threshold distortions, models of human vision are often employed, where the most prominent FR-VMs examples include: VDM [27], VDP [12], and HDR-VDP-2 [28]). In the specific task of predicting selected rendering and compression artifacts best performance has been achieved using machine learning [8] and CNN techniques [50].

No-reference metrics In this work we focus on the VMs due to locality of their prediction, but we are specifically interested in a challenging *no-reference* setup, where the reference image is not available. We discuss the most successful recent NR-IQMs that rely on machine learning techniques, and we refer the reader to a more complete metric surveys in [9, 24]. Early machine learning techniques employed predefined features such as SIFT and HOG [32, 31, 37, 43], and measured their distortions with respect to natural image statistics [47]. Recently CNN architectures are applied to such feature learning as well as the MOS regression at the same time [5, 21, 7, 42]. To compensate for a low number of MOS-labeled images, such solutions typically rely on patches, where they assign the same MOS score for all patches that belong to a given image [24]. Such practice is justified for specific classes of distortions that affect the whole image uniformly, which might be the case for certain types of image noise or compression artifacts, but might confuse the network in case of localized distortions such as those in IBR.

To compensate for the lack of true local reference image, Bosse et al. [7] learn the importance of local patches, but their key motivation is not in deriving the localized VM, but rather in estimating relative patch weights in the aggregated MOS rating. Lin and Wang [26] employ quality-aware generative network to hallucinate the reference image, which by employing adversarial learning is further refined by IQM-discriminator that is trained on ground truth references. Their hallucination-guided quality regression network is fed with the difference between the hallucinated and distorted images, as well as the distorted image itself to predict the MOS value. The quality-aware generative network, hallucination-guided quality regression network, and the IQM-discriminator are jointly optimised in an end-to-end manner. Kim and Lee [23] apply state-of-the-art FR-IQMs such as SSIM to generate proxy scores on patches as the ground truth to pre-train the model and then fine-tune their target NR-IQM. At intermediate stages the regression network considers mean values and the standard deviations of per-patch 100-element feature vectors which are then pooled to a per-image quality score.

In this work we also employ state-of-the-art FR-IQMs to perform an initial per-patch distortion annotation, and strike

the required balance between different error magnitudes in the training data, which is essential for meaningful training and shift-invariant properties of our NR-VM.

The research on NR-VMs is extremely sparse, presumably due to limited access to locally labeled images [18, 8, 50]. A notable exception is work of Herzog et al. [18] who employ support vector machines (SVM) to predict per-pixel distortions for selected rendering artifacts (they do not consider IBR) and achieve performance comparable to FR-VMs. In this work we demonstrate that time-consuming manual per-pixel distortion labeling is not strictly required.

Image-based rendering IBR for structured or unstructured light fields (LFs) of real-world scenes involves a number of computational steps such as: depth reconstruction, neighboring views warping, warped views blending, and disocclusion hole in-painting. Each of those steps is prone for inaccuracies that manifest themselves as IBR-specific artifacts such as object shifting (incorrect depth), crumbling, distorted edges (depth discontinuties, e.g. due to compression), popping (fluctuations in depth), ghosting (depth inaccuracy, view blending), stretching, blurry or black regions (in-painting) [44]. Specialized IBR quality metrics often rely on leaving one view out as the reference [46, 34, 41, 6] or searching for matching image blocks after their registration [3], and then employing customized FR-IQMs. NR-IQMs typically focus on detecting selected distortion types such as blurring and ghosting [4], ghosting and popping [15], blurring, stretching and black holes [44], and then aggregation of the final quality score as a combination of contributing distortions. Perceptual experiments are performed to understand how the observers rate the severity of different artifacts as a function of rendering parameters such as the number of blended views and viewing angles [45]. A skillful pre-processing of depth (e. g., depth blurring in uncertain regions) and choice of particular algorithmic solutions can substantially suppress artifacts [17], eventually using a neural network trained on IBR [16]. More objectionable distortion types can be traded-off to those that are more visually plausible (e. g., blurry depth that is more consistent but further from the ground truth).

All discussed work on IBR quality evaluation essentially focuses on providing a single score per-image, which also serves for their performance evaluation. While some FR-IQMs generate viable per-pixel VMs at indermediate stages [34, 41] their accuracy is not formally evaluated. The goal of this work is to pursue the NR-VM setup to detect local IBR distortions using CNN techniques.

3. Our approach

Overview Test-time input to our method is single distorted RGB image $\mathcal{A}$. Withheld is the clean RGB image $\mathcal{B}$. They are related as $\mathcal{A} = R(\mathcal{B})$, where R is the distortion operator such limited-quality IBR reconstruction. Output is a single-channel (scalar) image $\mathcal{A} \ominus \mathcal{B}$, where $\ominus$ is a difference metric such as MSE, SSIM [48] or VGG [40], that produces a high per-pixel value where the images are different and small values where they are similar. As it is important that the method reports errors (true positive) but also works on images without artifacts and correctly reports that there are no errors (true negative), we will balance the test and training data to avoid false positive and negatives.

3.1. Training data

Training data comprises of metric responses $\mathcal{A} \ominus \mathcal{B}$ to the distorted image $\mathcal{A}$ and the reference (clean) image $\mathcal{B}$. Strictly speaking, learning does not even observe the reference image $\mathcal{B}$, but in practice, it is required to compute the metric response $\mathcal{A} \ominus \mathcal{B}$.

Clean and distorted images come from 42 lightfield images, that come from the Stanford LF repository [1], Google Research work [33], and Technicolor [38] as well as from our own captures. All 4D LF data sets comprise of common 2D images in a resolution up to 2,000 px, taken from a range of sparse view points, such as in a 3×3 camera array with known view points. For each LF view point, we first estimate the depth using a light field depth estimation technique [11] and then warp [29] the image into the view of all others. For each LF, we use the four corner views to generate novel-view images from the remaining views. Each warped view corresponds to one original view, and we apply the metric to this pair. At ca. 9 views per LF and 42 LFs, this amounts to only 210 unique images, i. e., a comparatively low number.

We use six of these LF scenes for testing and the rest for training. The same split is applied later for the user study. Consequently, the learning did not only never see patches from the test set, but not even patches from the same scene. We think this is important as the number of scenes in the training set is small and generalization across them is an additional challenge.

Due to the inevitably low number of LF images, we additionally use natural images sourced from the Inria Holidays image dataset [20] which have comparable resolution to our LF images.

Our method is independent of the actual underlying metric $\ominus$ we predict. We will denote this response neutrally as $\mathcal{A} \ominus \mathcal{B}$. We experiment with three metrics: L2, SSIM and VGG16. L2 is defined as the average per-pixel RGB difference vector length squared. The SSIM metric is using the original implementation [48]. VGG16 [52] transforms both $\mathcal{A}$ and $\mathcal{B}$ into the VGG16 feature space and picks the activations at layer 5, which is 512-dimensional. The L_2 difference of these two vectors is used as the metric response. For each metric, we normalize the .95-percentile of their responses across the training dataset to fall between 0 and 1.

3.2. Architecture

We use a simple encoder [36] P, predicting the error when observing A, $P(A|\Theta)$ with learnable parameters Θ. It comprises of 5 layers (32×32 pacth size); the feature count is double in every layer with the total number of $|\Theta| = 175,537$ learnable parameters. The network is trained on all patches of the training set in a sliding window fashion.

The loss is the L_1 error of the predicted metrci response, so $||P(\mathcal{A}|\Theta) - (\mathcal{A} \ominus \mathcal{B})||_1$. Note that loss is always L_1, while metric can be the L-norm-like MSE as well SSIM or VGG16.

Balancing We have explained why, and will see from the ablation, that it is important to have natural patches, but the question is how many. If we take an unlimited number, the metric prediction simply always returns 0, because natural patches have no error to themselves. But how many is right?

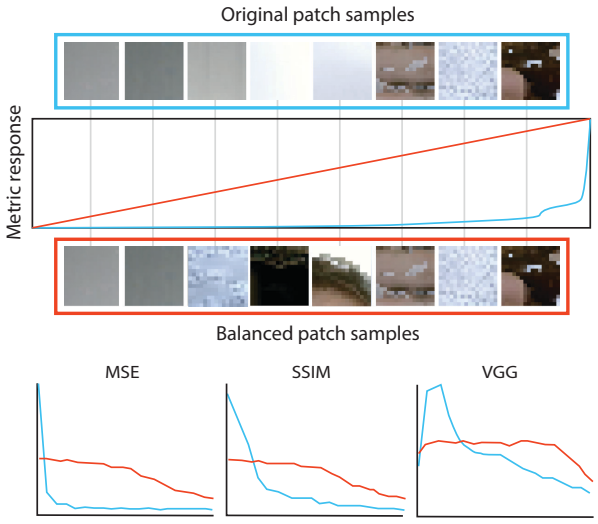

Figure 2. When sampling uniformly from IBR patches the error distribution is skewed towards low errors **(blue)**. Our balancing **(red)** adjusts the samples to have a uniform range of errors.The three lower plots show actual distribution before and after balancing for different metric responses.

Our solution is to take a half-half mix of distorted and clean patches. Regrettably, many of the distorted patches, which make 50 % of the total, also have errors similar close to zero. These patches are exactly those for which IBR was successful, i. e., did not result in artifacts. Depending on the metric, this imbalance can be very strong, and in particular for MSE, it is extremely heavy-tailed (Fig. 2). Addressing this, we balance the error distribution for the distorted half when creating the training data as follows: First we sort all patches by their metric response into a priority queue. Next, we uniformly random sample the range from 0 to the .95 percentile of the metric response distribution. For every sample i with value ξ_i, we find the patch j with the most similar metric response d_i and remove it from the queue and add it to the training data set. When the difference $\xi_i - d_j$ is larger than a threshold ϵ, we reject the sample. This is repeated until a target patch count such as 250 k is reached.

4. Evaluation

4.1. Methods

Strategies We compare three different strategies for training. The first is our, the other two are ablations. FULL is our complete method involving 50 % natural patches and a balancing of the other 50 % as described in Sec. 3.2. NOBALANCE is realized by a similar 50/50-split, but by training on all distorted patches without the balancing. NONATURAL applies the balancing to 100 % of patches coming from IBR without adding the natural patches as described in Sec. 3.2. All training sets. albeit processed differently, have the same size of ca. .5 M patches.

Error As we predict metric responses, our error is the same as the loss, the L_1 between the ground truth image metric response and our prediction of that response. As these errors also come in arbitrarily different scales for different metrics, we normalize them per metric by dividing by the global .95-percentile of the GT metric response across the balanced training data set.

We additionally report errors in metric prediction errors for a split subsets to understand the false/true-positive and false/true-negative tendency. First, all errors, same as the loss, are computed on the completed test data set (ALL). Additionally, we look into two sub-partitionings of the data. The first is CLEAN, which is the subset of all patches with strictly zero error, i. e., the natural patches. The second is DISTORTED that contains all the rest, i. e., the IBR patches, including those that might also come out with very low or even the "lucky few" with zero error. Note that this is a partitioning of the test set, which we also analyze, and not of the training set.

4.2. Quantitative results

We now discuss both the means and full error distributions of all methods on all partitions and all metrics.

Means The means of all methods are compared in Tbl. 1. We see that FULL error is smaller across the data set than both other variants (bold in column ALL).

In detail, when looking into the partitioning, we find that on the DISTORTED partition, the NONATURAL strategy performs best. This is expected as in the training 100 % of data comprised of a great variety of distorted patches with balanced error distribution. This makes the resulting metric particularly sensitive for all kinds of distortions. As a result

Table 1. Error of the metric predictions for different variants of our algorithms and different partitions (ALL/CLEAN/DISTORTED) of the training data **(columns)** on different metrics **(rows)**. Winners per-partition are marked bold.

Metric	FULL			NONATURAL			NOBALANCE		
	ALL	CLE.	DIST.	ALL	CLE.	DIST.	ALL	CLE.	DIST.
MSE	**.098**	.006	.189	.137	.092	**.182**	.102	**.003**	.201
SSIM	**.078**	.013	.143	.143	.159	**.127**	.080	**.012**	.149
VGG	**.085**	**.006**	.165	.207	.293	**.121**	.092	.008	.176

the probability of false negatives, i. e., claiming patches with an error to be fine, is low.

We also find, that for the CLEAN partition, the NOBALANCE strategy performs best. This also is expected as in the training 50 % of data comprised of natural (undistorted) patches, and due to the NOBALANCE strategy, small errors dominate in the distorted patches, which makes the resulting metric particularly sensitive for near-threshold distortions. As a result the probability of false positives, i. e., claiming patches without error to have a metric response, is low.

All statements are true across all metrics, indicating that FULL approach is independent of the underlying metric. A positive exception is VGG, where FULL approach even performs better than NOBALANCE also on the CLEAN partition.

All statements are significant ($p < .01$, t-test after Gaussianity testing).

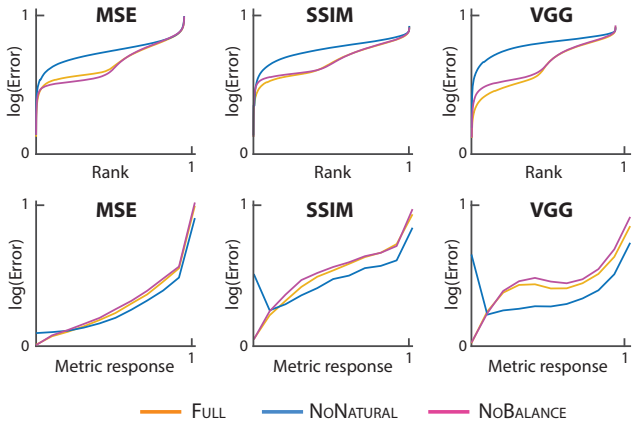

Figure 3. Analysis of metric prediction error, for different metrics and variants of our method. The top plots show sorted error distributions. The bottom row plots show the correlation of metric response and metric prediction error. All vertical axis are log scale.

Distributions In Fig. 3 we show the distribution of errors of the metric prediction (top) and the correlation of metric response and prediction error. In each plot, colors encode the variants of our approach (NONATURAL, NOBALANCE).

Each plot in the first row of Fig. 3 shows sorted error of our metric prediction, larger errors to the right. We see that across the entire range, with the exception of MSE prediction for low errors, the FULL approach performs better than other variants. This indicates, that the mean is a good characterization of the performance. In all cases we note an increase in error around 50 % of the population. We hypothesize, that these are the patches that are (partially) not aligned between reference and input. There is no way to tell apart an unaligned patch which is otherwise fine, that is judged by FR metrics as different in respect to a displaced reference. So large errors are expected to become undetectable at some error level. The exception is the regime in MSE where the FULL approach, which performs best on average (Tbl. 1), is worse on low errors and slightly better on high errors. This can be difficult to comprehend due to the log scale of the vertical axis.

Each plot in the second row in Fig. 3 shows the error of our prediction on the vertical axis and the metric response on the horizontal axis as a connected scatter plot. A method that is better on the left is better at correctly predicting low metric response. A method that is better on the right is more suited to deal with high metric responses. We see the picture is in agreement with Tbl. 1: The NONATURAL method has a high error on patches with small metric response (false positives). Symmetrically, the NOBALANCE method has a high error on patches with high metric response (false negatives). FULL method is always a bit worse than one other method for one regime (except at the unique point where both cross), but on average performs best overall.

4.3. Qalitative results

Example metric outputs Fig. 4 shows an analysis of the response of all metrics to two different LFs from the test set. The first column shows the distorted input $\mathcal{A}$ in the top, below the hidden reference $\mathcal{B}$ and below this three insets from both. The second row shows our predicted response $\mathcal{A} \ominus \mathcal{B}$ for different metrics: MSE on top, followed by SSIM and VGG. A false color coding, where cold colors indicate a low response and warm colors indicate a high response, is used. The third row shows the GT response for the same. We note, that the similarity exists between our prediction and the GT. We slightly err towards conservative, i. e., miss a few errors. How some of these errors are only false findings, i. e., a limitation of the metrics, becomes apparent from the user study to follow.

The last column shows a sanity check where we put the hidden reference image $\mathcal{B}$ into our metric. Such an image does not have any error, and consequently reporting any error is a false positive. We see, that our image has a few sporadic responses in areas that are correct but look like IBR artifacts, but in most areas has no response. In summary, this indicates we localize and scale error to a hidden reference

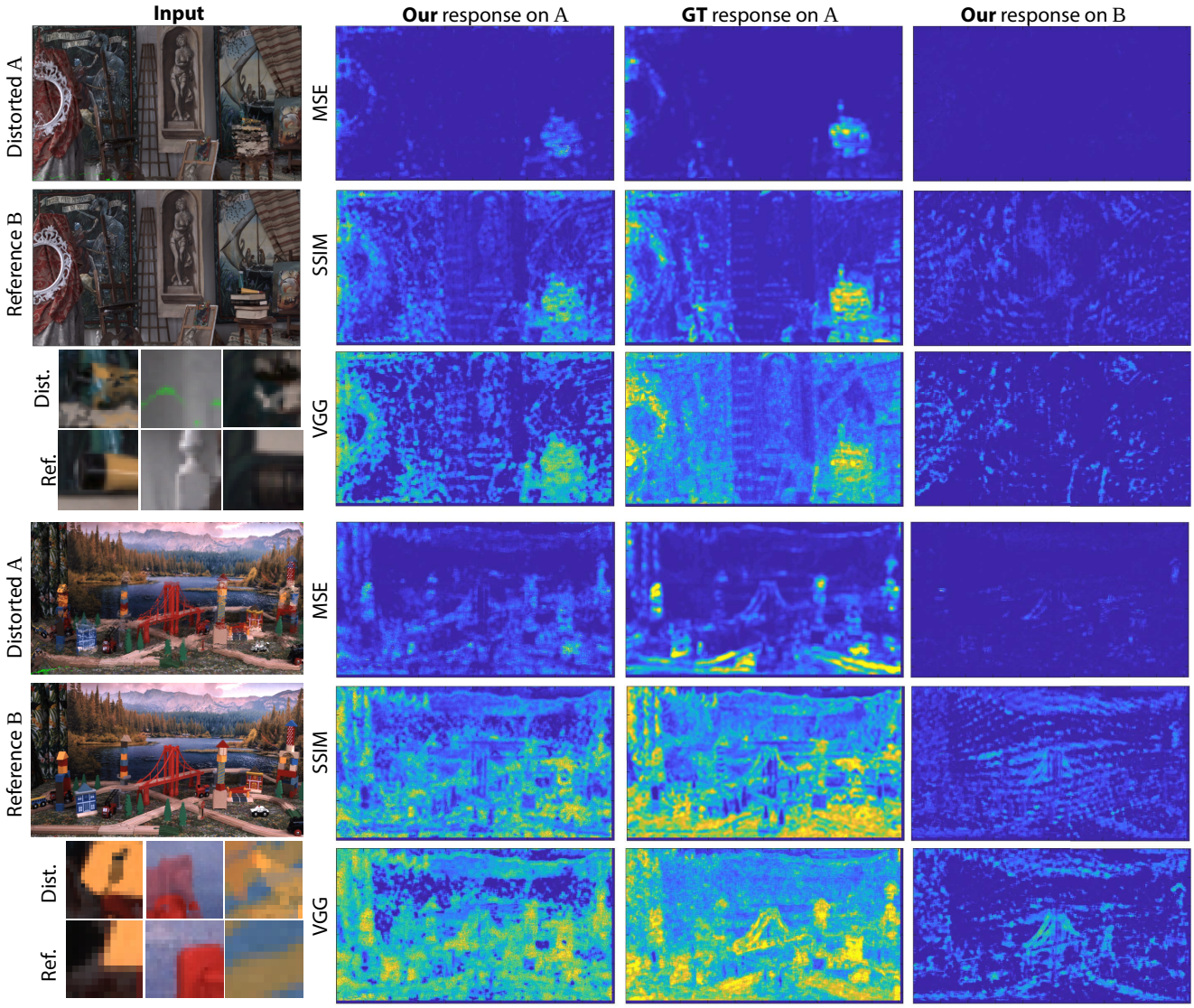

Figure 4. Comparing the response to a pair of an image A and its distorted version B **(first column)**. Our response **(second column)** is similar to the ground truth **(third column)**. When executed on the clean reference **(fourth colum)**, only very few false positives are reported.

in images with artifacts, while avoiding to produce a signal when facing clean images. It might appear that MSE has less false positives than SSIM or VGG when inspecting the last column; simply less blue, very close to perfect in the first row. However, such a trend is not supported by the numbers in Tbl. 1 or the plots in Fig. 3. The true reason for this impression might be that the SSIM and VGG response simply have a larger receptive field per-se: MSE is per-pixel while VGG is affected by up 16×16 pixels. Even the ground truth response is more dense (less blue). Consequently the metric prediction, if in error, also makes spatially more extended, more dense, mistakes.

Transformation-invariance Surprisingly, results produced by our approach can turn out to be better than their own supervision, as our method is forced to come up with strategies to detect problems without seeing the reference. This makes it immune to a common issue of many image metrics: misalignment [22]. Even a simple shift in image content, will result in many false positives for classic metrics (Fig. 5). An image that has merely been shifted is reported to be very different from a reference by all the metrics used for our supervision. Not much changes if we add IBR artifacts to it. Our method however does not care about transformation, still, when IBR artifacts are added, they are detected. Our method however, does not see the reference, and is not subject to such a misconception. While not quantifiable, the result qualitatively is arguably more similar to human judgment, as indicated by the user experiment in the next subsection.

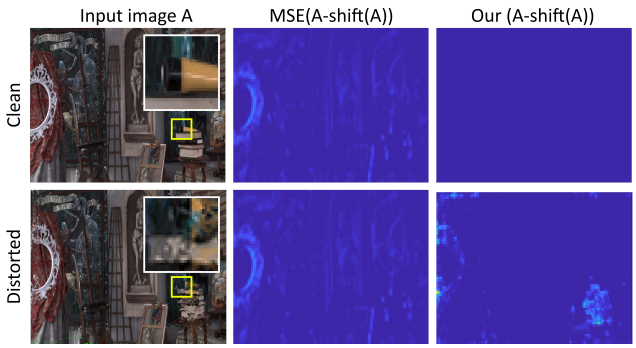

Figure 5. Shift-invariance of our approach: When computing the distance between an input image $\mathcal{A}$ **(first column, first row)** and a misaligned reference $\mathcal{B}$ (not shown, 20-px shifted copy of $\mathcal{A}$), a common metric such as MSE will show a strong response **(first row, second column)**, which is numerically correct, but far from human assessment, which would be more similar to our response **(first row, last column)** i. e., no difference. Symmetrically, repeating the experiment on a distorted input and a shifted copy of this input, our approach correctly localizes the distortions around the books (inset) as if the reference had been aligned.

4.4. User study

We have conducted a user experiment to validate that our predicted metric responses spatially correlate with the visibility of artifacts to human subjects. As the experiment outcome we require per-pixel annotated (i. e., painted) error maps for IBR artifacts. Note, that none of the user responses were used for training.

Methods Naïve users were asked to use a binary painting interface to mark errors in a view-interpolation image for each of the six LFs of our test data set in an open-ended session that took 15 minutes on average. We average the binary response into a continuous fraction (percentage) of users that detected the location to be an artifact.

Analysis Asking $N = 10$ users, we find the correlation (Pearson linear correlation R, higher values are better; statements highly significant as the correlation is computed on a high number of image pixels) reported in Fig. 6, b. We see that for many scenes (14 out of 21), as well as for the average across scenes, our method has a higher correlation with user annotation than the metric it was supervised on. We hypothesize, that this is due to the fact that our network had learned to become independent of a reference, a similar robustness that the HVS employs. There is no clear trend on which of our metric response predictions correlates more with user annotation. The differences between scenes however seem more pronounced.

When repeating the experiment with a non-aligned reference (shifted a mere 20 px to the right), we find the correlations reported in Fig. 6, c. We see that our correlation

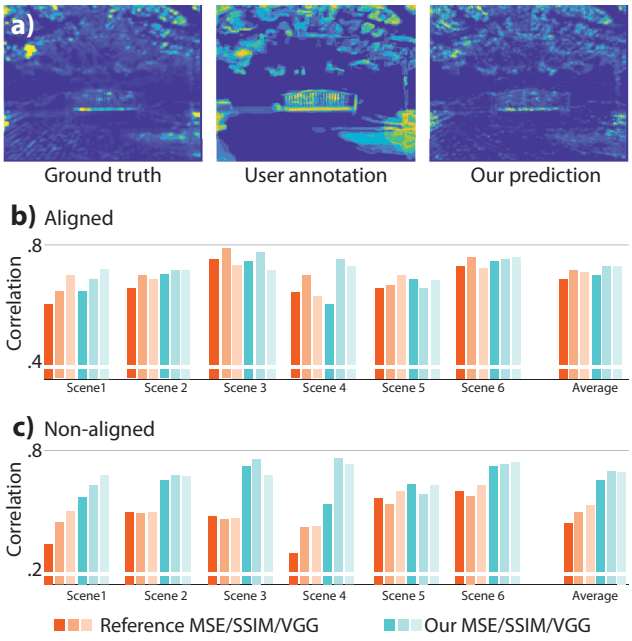

Figure 6. Example user study result **(top)**. Correlation (significant, $p < .001$) of MSE/SSIM/VGG and user responses (red) compared to our predictions of these (blue) for different scenes and as an average across scenes on the right **(middle)**. In the non-aligned conditions, these differences get stronger **(top)**.

even improves in this condition (we win in 21 of 21 comparisons), showing we are more robust to alignment issues when predicting user responses.

Perceptualization Finally, as computing linear correlation (R) involves fitting a model $x_i = a \cdot y_i + b$ where x_i is the user response and y_i is our prediction of the metric response for pixel i. This allows a "perceptualization" of our metrics response. Fitting multiple models a, b in a leave-one-out protocol to 5 of our 6 images produces an average error of $.05/.04/.02$ for MSE/SSIM/VGG, indicating that this perceptualization generalizes to an extend.

4.5. Other atchitectures

We also explored using other architectures with or without balancing. A simple solution would be to use an supervised image translation network such as Pix2Pix [19] to map from entire IBR images to the metric response. Regrettably, training these on our data set converges to a flat response of zero, as artifacts are too rare and subtle to be picked without the balancing we suggest. Future work could investigate combining our balancing with other network architectures.

5. Conclusion

We have demonstrated that with properly adjusted training data (prioritization and natural supervision), a CNN can

learn how to predict the difference of an image to a hidden reference. Our approach is independent of the metric used and we have shown L2, SSIM and VGG prediction. Other metrics such as HDR-VDP-2 [28] or the CNN-based metric of Wolski et al. [50] would likely be predictable in a similar fashion.

In future work, we would like to overcome the limitations to paired input, eventually using an adversarial [13] design, and learn the prediction only from pairs and without the metric, or only from pairs of undistorted-metric or distorted-metric.

References

[1] http://lightfield.stanford.edu/lfs.html. 3

[2] S. A. Amirshahi, M. Pedersen, and S. X. Yu. Image quality assessment by comparing cnn features between images. *J Imag. Sci. and Technology*, 60(6):60410–1, 2016. 2

[3] F. Battisti, E. Bosc, M. Carli, P. Le Callet, and S. Perugia. Objective image quality assessment of 3d synthesized views. *Image Commun.*, 30(C):78–88, 2015. 3

[4] K. Berger, C. Lipski, C. Linz, A. Sellent, and M. Magnor. A ghosting artifact detector for interpolated image quality assessment. In *IEEE Int. Symp. on Consumer Electronics*, pages 1–6, 2010. 3

[5] S. Bianco, L. Celona, P. Napoletano, and R. Schettini. On the use of deep learning for blind image quality assessment. *arXiv:1602.05531*, 2016. 2

[6] E. Bosc, R. Pepion, P. L. Callet, M. Koppel, P. Ndjiki-Nya, M. Pressigout, and L. Morin. Towards a new quality metric for 3-d synthesized view assessment. *IEEE J of Selected Topics in Signal Processing*, 5(7):1332–1343, 2011. 3

[7] S. Bosse, D. Maniry, K. R. Müller, T. Wiegand, and W. Samek. Deep neural networks for no-reference and full-reference image quality assessment. *IEEE TIP*, 27(1):206–219, 2018. 2

[8] M. Čadík, R. Herzog, R. Mantiuk, R. Mantiuk, K. Myszkowski, and H.-P. Seidel. Learning to predict localized distortions in rendered images. In *Comp. Graph. Forum*, volume 32, pages 401–10, 2013. 2, 3

[9] D. M. Chandler. Seven challenges in image quality assessment: Past, present, and future research. *ISRN Signal Processing*, 2013. 2

[10] S. Coleman. www.theliteratelens.com: Magnum and the dying art of darkroom printing, 2012. 1

[11] Ł. Dabała, M. Ziegler, P. Didyk, F. Zilly, J. Keinert, K. Myszkowski, H.-P. Seidel, P. Rokita, and T. Ritschel. Efficient Multi-image Correspondences for On-line Light Field Video Processing. *Comp. Graph. Forum (Proc. PG)*, 2016. 3

[12] S. J. Daly. Visible differences predictor: an algorithm for the assessment of image fidelity. In *Human Vision, Visual Processing, and Digital Display III*, volume 1666, pages 2–16. International Society for Optics and Photonics, 1992. 2

[13] I. Goodfellow, J. Pouget-Abadie, M. Mirza, B. Xu, D. Warde-Farley, S. Ozair, A. Courville, and Y. Bengio. Generative adversarial nets. In *Advances in neural information processing systems*, pages 2672–2680, 2014. 8

[14] S. J. Gortler, R. Grzeszczuk, R. Szeliski, and M. F. Cohen. The lumigraph. In *SIGGRAPH*, pages 43–54, 1996. 2

[15] S. Guthe, P. Schardt, M. Goesele, and D. Cunningham. Ghosting and popping detection for image-based rendering. In *Proc. 3DTV*, pages 1–4, 2016. 3

[16] P. Hedman, J. Philip, T. Price, J.-M. Frahm, G. Drettakis, and G. J. Brostow. Deep blending for free-viewpoint image-based rendering. *ACM Trans. Graph. (Proc. SIGGRAPH)*, 37(6), 2018. 3

[17] P. Hedman, T. Ritschel, G. Drettakis, and G. Brostow. Scalable inside-out image-based rendering. *ACM Trans. Graph. (Proc. SIGGRAPH Asia)*, 35(6), 2016. 3

[18] R. Herzog, M. Čadík, T. O. Aydin, K. I. Kim, K. Myszkowski, and H.-P. Seidel. NoRM: No-reference image quality metric for realistic image synthesis. *Comp. Graph. Forum*, 31(2):545–54, 2012. 3

[19] P. Isola, J.-Y. Zhu, T. Zhou, and A. A. Efros. Image-to-image translation with conditional adversarial networks. *arxiv*, 2016. 7

[20] H. Jégou, M. Douze, and C. Schmid. Hamming embedding and weak geometry consistency for large scale image search-extended version. 2008. 3

[21] L. Kang, P. Ye, Y. Li, and D. Doermann. Convolutional neural networks for no-reference image quality assessment. In *CVPR*, pages 1733–40, 2014. 2

[22] P. Kellnhofer, T. Ritschel, K. Myszkowski, and H.-P. Seidel. Transformation-aware perceptual image metric, 2016. 1, 6

[23] J. Kim and S. Lee. Fully deep blind image quality predictor. *IEEE J Sel. Topics in Signal Processing*, 11(1):206–220, 2017. 2

[24] J. Kim, H. Zeng, D. Ghadiyaram, S. Lee, L. Zhang, and A. C. Bovik. Deep convolutional neural models for picture-quality prediction: Challenges and solutions to data-driven image quality assessment. *IEEE Signal Processing Magazine*, 34(6):130–141, 2017. 2

[25] M. Levoy and P. Hanrahan. Light field rendering. In *SIGGRAPH*, pages 31–42, 1996. 2

[26] K. Y. Lin and G. Wang. Hallucinated-iqa: No-reference image quality assessment via adversarial learning. *CVPR*, 2018. 2

[27] J. Lubin. *Vision Models for Target Detection and Recognition*, chapter A Visual Discrimination Model for Imaging System Design and Evaluation, pages 245–283. World Scientific, 1995. 2

[28] R. Mantiuk, K. J. Kim, A. G. Rempel, and W. Heidrich. HDR-VDP-2: a calibrated visual metric for visibility and quality predictions in all luminance conditions. *ACM Trans. Graph. (Proc. SIGGRAPH)*, 2011. 2, 8

[29] W. R. Mark, L. McMillan, and G. Bishop. Post-rendering 3D warping. In *Proc. i3D*, 1997. 3

[30] L. McMillan and G. Bishop. Plenoptic modeling: An image-based rendering system. In *SIGGRAPH*, pages 39–46, 1995. 2

[31] A. Moorthy and A. Bovik. A two-step framework for constructing blind image quality indices. *IEEE Signal Proc. Letters*, 17(5):513–16, 2010. 2

[32] M. Narwaria and W. Lin. Objective image quality assessment based on support vector regression. *IEEE Trans. Neural Networks*, 21(3):515–9, 2010. 2

[33] E. Penner and L. Zhang. Soft 3d reconstruction for view synthesis. 36(6), 2017. 3

[34] L. M. Pierre-Henri Conze, Philippe Robert. Objective view synthesis quality assessment. In *Proc. SPIE*, 2012. 3

[35] N. Ponomarenko, V. Lukin, A. Zelensky, K. Egiazarian, M. Carli, and F. Battisti. TID2008 - A database for evaluation of full-reference visual quality assessment metrics. *Advances of Modern Radioelectronics*, 10:30–45, 2009. 2

[36] O. Ronneberger, P.Fischer, and T. Brox. U-Net: Convolutional networks for biomedical image segmentation. In *MICCAI*, pages 234–241, 2015. 4

[37] M. Saad, A. Bovik, and C. Charrier. Blind image quality assessment: A natural scene statistics approach in the DCT domain. *IEEE TIP*, 21(8):3339–3352, 2012. 2

[38] N. Sabater, G. Boisson, B. Vandame, P. Kerbiriou, F. Babon, M. Hog, T. Langlois, R. Gendrot, O. Bureller, A. Schubert, and V. Allie. Dataset and pipeline for multi-view light-field video. In *CVPR Workshops*, 2017. 3

[39] H. Sheikh, M. Sabir, and A. Bovik. A statistical evaluation of recent full reference image quality assessment algorithms. *IEEE TIP*, 15(11):3440–3451, 2006. 2

[40] K. Simonyan and A. Zisserman. Very deep convolutional networks for large-scale image recognition. *arXiv:1409.1556*, 2014. 1, 3

[41] M. Solh, G. AlRegib, and J. M. Bauza. 3VQM: a vision-based quality measure for dibr-based 3D videos. In *2011 IEEE Int. Conf. on Multimedia and Expo*, pages 1–6, 2011. 3

[42] H. Talebi and P. Milanfar. Nima: Neural image assessment. *IEEE TIP*, 27(8):3998–4011, 2018. 1, 2

[43] H. Tang, N. Joshi, and A. Kapoor. Learning a blind measure of perceptual image quality. *CVPR*, pages 305–12, 2011. 2

[44] S. Tian, L. Zhang, L. Morin, and O. Dforges. NIQSV+: A no-reference synthesized view quality assessment metric. *IEEE TIP*, 27(4):1652–64, 2018. 3

[45] P. Vangorp, G. Chaurasia, P.-Y. Laffont, R. W. Fleming, and G. Drettakis. Perception of visual artifacts in image-based rendering of façades. In *Comp. Graph. Forum*, volume 30, pages 1241–50, 2011. 3

[46] M. Waechter, M. Beljan, S. Fuhrmann, N. Moehrle, J. Kopf, and M. Goesele. Virtual rephotography: Novel view prediction error for 3d reconstruction. *ACM Trans. Graph.*, 36(1), 2017. 3

[47] Z. Wang and A. C. Bovik. *Modern Image Quality Assessment*. Morgan & Claypool Publishers, 2006. 2

[48] Z. Wang, A. C. Bovik, H. R. Sheikh, and E. P. Simoncelli. Image quality assessment: from error visibility to structural similarity. *IEEE TIP*, 13(4):600–12, 2004. 1, 3

[49] L. Williams. Casting curved shadows on curved surfaces. *SIGGRAPH Comput. Graph.*, 12(3):270–4, 1978. 1

[50] K. Wolski, D. Giunchi, N. Ye, P. Didyk, K. Myszkowski, R. Mantiuk, H.-P. Seidel, A. Steed, and R. K. Mantiuk. Dataset and metrics for predicting local visible differences. *ACM Trans. Graph.*, 2018. 2, 3, 8

[51] L. Zhang, L. Zhang, X. Mou, and D. Zhang. FSIM: A feature similarity index for image quality assessment. *IEEE TIP*, 20(8):2378–2386, 2011. 2

[52] R. Zhang, P. Isola, A. A. Efros, E. Shechtman, and O. Wang. The unreasonable effectiveness of deep features as a perceptual metric. *CVPR*, 2018. 1, 2, 3

[53] X. Zhang and B. A. Wandell. A spatial extension of CIELAB for digital color-image reproduction. *J ISD*, 5(1):61, 1997. 2